Phonon-Induced Population Dynamics and Intersystem Crossing in Nitrogen-Vacancy Centers

M. L. Goldman,[1,*] A. Sipahigil,[1] M. W. Doherty,[2] N. Y. Yao,[1] S. D. Bennett,[1] M. Markham,[3] D. J. Twitchen,[3] N. B. Manson,[2] A. Kubanek,[1] and M. D. Lukin[1]

[1]*Department of Physics, Harvard University, Cambridge, Massachusetts 02138, USA*

[2]*Laser Physics Centre, Research School of Physics and Engineering, Australian National University, Australian Capital Territory 0200, Australia*

[3]*Element Six Ltd, Kings Ride Park, Ascot SL5 8BP, United Kingdom*

(Received 13 June 2014; revised manuscript received 16 December 2014; published 8 April 2015)

We report direct measurement of population dynamics in the excited state manifold of a nitrogen-vacancy (NV) center in diamond. We quantify the phonon-induced mixing rate and demonstrate that it can be completely suppressed at low temperatures. Further, we measure the intersystem crossing (ISC) rate for different excited states and develop a theoretical model that unifies the phonon-induced mixing and ISC mechanisms. We find that our model is in excellent agreement with experiment and that it can be used to predict unknown elements of the NV center's electronic structure. We discuss the model's implications for enhancing the NV center's performance as a room-temperature sensor.

DOI: 10.1103/PhysRevLett.114.145502 PACS numbers: 63.20.kd, 42.50.Md, 63.20.kp, 78.47.-p

The nitrogen-vacancy (NV) center in diamond has emerged as a versatile atomlike system, finding diverse applications in metrology and quantum information science at both ambient and cryogenic temperatures. At room temperature, the NV center has broad appeal as a sensor—e.g., for nanoscale, biocompatible thermometry [1], magnetometry [2], pressure sensing [3], and electric field sensing [4]. NV centers also have the potential to serve as quantum registers featuring high-fidelity quantum gates [5] and second-long coherence times [6]. All of these applications depend critically on a spin-dependent nonradiative transition into a metastable state, the so-called intersystem crossing (ISC), which enables nonresonant optical initialization and readout of the electronic spin state. Despite theoretical [7] and experimental [7–10] efforts, a detailed understanding of the microscopic ISC mechanism has remained an open question. Such an understanding may enable efforts to enhance the NV center's optical initialization and readout fidelities, or to identify or engineer similar mechanisms in other solid-state defects.

In this Letter, we use resonant optical manipulation of an NV center at cryogenic temperatures to probe the NV center's interaction with phonons in the diamond lattice. The NV center has a spin-triplet, orbital-singlet ground state ($^3A_2$) that is coupled optically to a spin-triplet, orbital-doublet excited state (^3E), as shown in Fig. 1(a). We investigate the ISC from the ^3E manifold to the intermediate spin-singlet states ($|^1A_1\rangle$, $|^1E_{1,2}\rangle$) and phonon-mediated population transfer within the ^3E manifold. We first measure phonon-induced population transfer between $|E_x\rangle$ and $|E_y\rangle$, using the effectively closed three-level system shown in Fig. 1(b), to characterize phononic coupling to the orbital electronic state. We build on previous such measurements [11,12], in which population transfer was not shown to be completely suppressed, by adopting techniques that enable highly coherent excitation of the NV center's optical transitions [13,14].

We next measure the fluorescence lifetimes of $|A_1\rangle$, $|A_2\rangle$, and $|E_{1,2}\rangle$ and find that the ISC rates from these states differ sharply. Based on these experimental observations, we develop a model of the ISC mechanism that combines spin-orbit coupling, phonon-induced electronic state transitions, and phonon-mediated lattice relaxation. Using our measured phonon-induced mixing rate as an input, we find

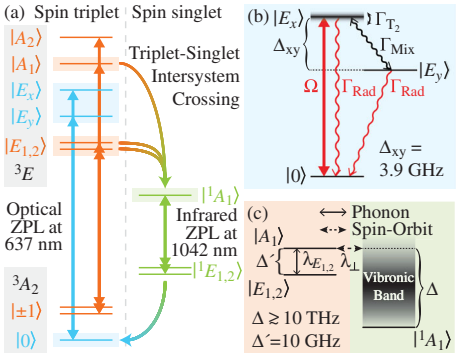

FIG. 1 (color). The level structure of the NV center. (a) A schematic illustration of the NV center's level structure. The intersystem crossing (ISC) process is responsible for shelving into $|^1E_{1,2}\rangle$ via the short-lived $|^1A_1\rangle$ and for pumping into $|0\rangle$. (b) The three-level system of spin-triplet, $m_s = 0$ states used to model phonon-induced mixing and dephasing within the ^3E manifold. (c) The states, Hamiltonian matrix elements ($\lambda_{E_{1,2}}$, $\lambda_\perp$), and energy scales (Δ, Δ') involved in the triplet-singlet ISC.

excellent quantitative agreement between our model, our experimental results, and previous observations [7–10].

In our experiment, we use a 1.0 mm diameter solid-immersion lens (SIL) that is fabricated from bulk electronic grade CVD diamond and cut along the (100) crystal plane [15]. The SIL is mounted in a continuous flow helium cryostat that allows us to vary the temperature from 4.8 K to room temperature. We use a laser at 532 nm for nonresonant initialization of the NV center's charge and spin states, and two tunable external-cavity diode lasers gated by electro-optical amplitude modulators to apply independent resonant pulses at 637 nm. Using photoluminescence excitation (PLE) spectroscopy, we resolve five of the six dipole-allowed $^3A_2 \rightarrow {}^3E$ transitions; at zero applied magnetic field and low strain, $|E_1\rangle$ and $|E_2\rangle$ are too close in energy for their transitions from $|\pm 1\rangle$ to be resolved.

To measure the mixing rate between $|E_x\rangle$ and $|E_y\rangle$, we measure both the decay rate out of one of the states and the rate of population transfer between the two states. First, we measure the decay rate out of $|E_x\rangle$ by measuring the time scale τ_{Rabi} on which optical Rabi oscillations between $|0\rangle$ and $|E_x\rangle$ decohere. We apply resonant 60 ns pulses and record the arrival times of the resulting phonon sideband (PSB) photons, as the rate of spontaneous emission into the PSB is instantaneously proportional to the population in $|E_x\rangle$ and $|E_y\rangle$ [13,16].

For each data set, we fit τ_{Rabi} from the oscillation decay and extract $\Gamma_{\mathrm{Rad}} = 1/\tau_{\mathrm{Rad}}$ from the pulse's falling edge, where τ_{Rad} is the radiative lifetime of $|E_x\rangle$. From these two values, we extract

$$\Gamma_{\mathrm{Add}} = \Gamma_{\mathrm{Mix}} + \Gamma_{T_2} = 2\left(1/\tau_{\mathrm{Rabi}} - \frac{3}{4}\Gamma_{\mathrm{Rad}}\right), \qquad (1)$$

the additional decoherence rate of the Rabi oscillations due to processes other than optical decay to $|0\rangle$ [16,21]. Γ_{Mix} and Γ_{T_2} are the phonon-induced mixing and dephasing rates, respectively. Typical Rabi oscillations and the derived values of Γ_{Add} are shown in Fig. 2(a). The T^5 scaling of Γ_{Add} indicates that the additional Rabi decoherence is due primarily to mixing between $|E_x\rangle$ and $|E_y\rangle$ mediated by two E-symmetric phonons [11,22]. We infer $\Gamma_{\mathrm{Add}}/2\pi = -0.34 \pm 1.87$ MHz at 5.8 K (95% confidence interval), indicating that phonon-induced mixing is frozen out at low temperature. There also exists a one-phonon emission process whose contribution to the mixing rate scales as $\Delta_{xy}^2 T$ [22]. This contribution is negligible in our experiment because of the small density of states for phonons of frequency $\Delta_{xy} = 3.9$ GHz [23].

We also measure population transfer between $|E_x\rangle$ and $|E_y\rangle$ directly by measuring the depolarization of the emitted zero-phonon line (ZPL) fluorescence. ZPL photons emitted by decay from the $|E_x\rangle$ and $|E_y\rangle$ states have orthogonal linear polarizations (labeled x and y). At 5 and 20 K, we resonantly excite the NV center to $|E_x\rangle$ and collect fluorescence of x and y polarizations, as shown in Fig. 2(b). At

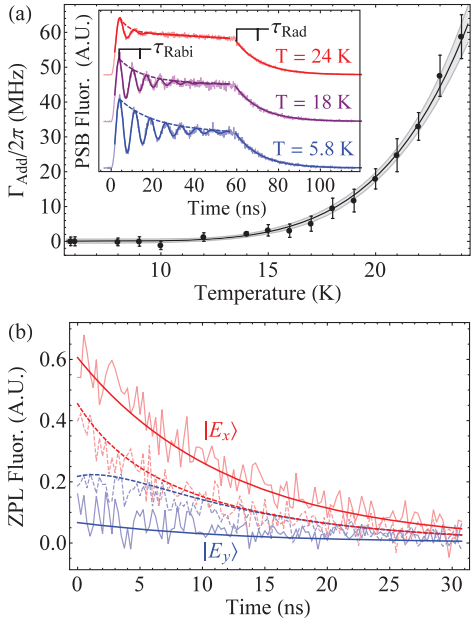

FIG. 2 (color). Phonon-induced mixing between the $|E_x\rangle$ and $|E_y\rangle$ electronic orbital states. (a) The measured $\Gamma_{\mathrm{Add}} = \Gamma_{\mathrm{Mix}} + \Gamma_{T_2}$ as a function of temperature, with a fit to $\Gamma_{\mathrm{Add}} \propto T^5$ [16]. The shaded region is the 95% confidence interval and the inset shows Rabi oscillations on the $|0\rangle \rightarrow |E_x\rangle$ transition measured at three temperatures, offset for clarity. (b) Background-subtracted fluorescence of x (red) or y (blue) polarization collected after resonant excitation to $|E_x\rangle$. Data were taken at $T = 5.0$ K (solid lines) and $T = 20$ K (dashed lines). The fits are simulations to the three-level system depicted in Fig. 1(b) [16].

both temperatures, the emission is x polarized for small delays, indicating initial decay primarily from $|E_x\rangle$. The emission remains x polarized at 5 K, whereas we observe that emission becomes depolarized at 20 K. Since emission polarization is directly related to the excited state population, this is a direct observation of population transfer between $|E_x\rangle$ and $|E_y\rangle$. We compare the observed population transfer to simulations of rate equations based on the three-level system depicted in Fig. 1(b) [16]. Using the values of Γ_{Add} given by the fit in Fig. 2(a), and using our polarization selectivity and the starting time of the mixing and radiative decay dynamics relative to the excitation pulse as fit parameters, we find good agreement between the observed and simulated fluorescence depolarization [16].

We now turn from the ^3E states with $m_s = 0$ ($|E_x\rangle$ and $|E_y\rangle$) to the states with $|m_s| = 1$ ($|A_1\rangle$, $|A_2\rangle$, and $|E_{1,2}\rangle$). Although the radiative decay rate Γ_{Rad} is the same for all $^3E \rightarrow {}^3A_2$ transitions [8,9], one expects from symmetry arguments that $|A_1\rangle$, $|A_2\rangle$, and $|E_{1,2}\rangle$ should exhibit different ISC rates into the spin-singlet states [24]. We can therefore probe population dynamics among these states by exciting the NV center into one state and measuring the decay time of the resulting PSB fluorescence as a function of temperature. A representative measurement is shown in the inset to Fig. 3. From the fluorescence decay time τ_i

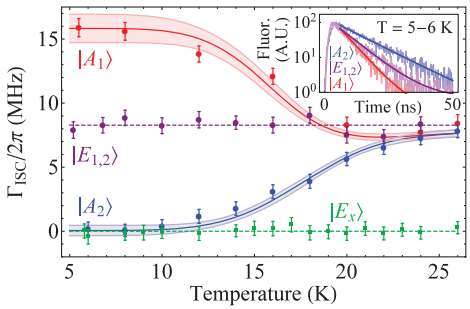

FIG. 3 (color). ISC rates from the ^3E triplet excited states. The inset shows the measured PSB fluorescence collected after excitation to $|A_1\rangle$, $|A_2\rangle$, and $|E_{1,2}\rangle$ measured at $T \sim 5$ K, normalized to a common peak height and fit to an exponential decay curve. The blue and red bands are fits with 95% confidence intervals to the phonon-induced mixing model described in the text, and the purple and green lines are placed at the mean values of the corresponding data sets.

measured after excitation into the ith state, we can calculate the associated ISC rate

$$\Gamma_i = 1/\tau_i - \Gamma_{\mathrm{Rad}}. \tag{2}$$

Because the ISC rates from $|E_x\rangle$ and $|E_y\rangle$ are negligible ($\Gamma_{E_x}/2\pi \leq 0.62 \pm 0.21$ MHz [16]) compared to the ISC rates from $|A_1\rangle$, $|A_2\rangle$, and $|E_{1,2}\rangle$, we set $\Gamma_{\mathrm{Rad}}/2\pi = 1/2\pi\bar{\tau}_{E_x} = 13.2 \pm 0.5$ MHz, where $\bar{\tau}_{E_x}$ is the average lifetime of $|E_x\rangle$ extracted from our Rabi decoherence data. The derived values of Γ_i are shown in Fig. 3.

We observe that the $|A_1\rangle$, $|A_2\rangle$, and $|E_{1,2}\rangle$ ISC rates are significantly different at low temperatures, but converge around $T \gtrsim 22$ K. The same two-phonon process that redistributes population among $|E_x\rangle$ and $|E_y\rangle$ also does so among $|A_1\rangle$ and $|A_2\rangle$. As a result, the observed temperature-dependent ISC rates ($\tilde{\Gamma}_{A_1}$ and $\tilde{\Gamma}_{A_2}$) converge to an average of the two unmixed states' rates (Γ_{A_1} and Γ_{A_2}) as the temperature increases. We fit $\tilde{\Gamma}_{A_1}$ and $\tilde{\Gamma}_{A_2}$, assuming $\Gamma_{A_2} = 0$ and a temperature-dependent $|A_1\rangle - |A_2\rangle$ mixing rate equal to the measured $|E_x\rangle - |E_y\rangle$ rate [16]. We find excellent agreement using only Γ_{A_1} as a free parameter, confirming that the same phonon-induced mixing process is evident in both Figs. 2 and 3. The state lifetimes we observe at $T \geq 22$ K are consistent with those of the $m_s = 0$ and $|m_s| = 1$ states at room temperature [see Fig. 4(c)], indicating that we have measured the onset of the orbital averaging mechanism that enables the ^3E manifold to be treated as an effective spin-triplet, orbital-singlet system at room temperature [25,26].

We now present a theoretical analysis of the ISC mechanism, which is treated in greater detail in Ref. [22]. In the NV center, an axial spin-orbit (SO) interaction ($\propto \lambda_{||} l_z s_z$) is primarily responsible for the fine structure of the ^3E manifold while a transverse SO interaction [$\propto \lambda_\perp (l_x s_x + l_y s_y)$] couples states of different spin multiplicities [27,28]. The ISC occurs in two steps [see Fig. 1(c)]: (i) a SO-mediated transition from a state in the ^3E manifold to a resonant excited vibrational level of $|^1A_1\rangle$, and (ii) relaxation of the excited vibrational level to the ground (or thermally occupied) vibrational level of $|^1A_1\rangle$. Because the latter occurs on the picosecond time scale [29], the overall ISC rate is defined by the initial SO-mediated transition.

According to Fermi's golden rule, the SO-mediated transition requires both SO coupling and overlap between the initial vibrational level of ^3E and the excited vibrational level of $|^1A_1\rangle$. Because $|^1A_1\rangle$ and the $^3A_2$ states consist of the same single-particle electronic orbitals, the two states exhibit similar charge density distributions and therefore similar vibrational potentials [30]. The vibrational overlap between the ^3E states and $|^1A_1\rangle$ is then well approximated by that observed in the PSB of the $^3E \rightarrow {}^3A_2$ optical emission spectrum. Selection rules imply that only $|A_1\rangle$ is SO coupled with $|^1A_1\rangle$. Thus, SO coupling can mediate a first-order transition from $|A_1\rangle$ to a resonant excited vibrational level of $|^1A_1\rangle$, whereas $|E_{1,2}\rangle$ must undergo a second-order transition involving electron-phonon coupling with $|A_1\rangle$ [see Fig. 1(c)]. In principle, $|E_{1,2}\rangle$ may undergo a first-order transition to a highly excited vibrational level of $|^1E_{1,2}\rangle$, but we expect the rate of this transition to be negligible because the $|^1A_1\rangle - |^1E_{1,2}\rangle$ energy spacing (1190 meV [31]) is large compared to the extent of the PSB (~500 meV [30,32]).

The ISC rate from $|A_1\rangle$ is

$$\begin{aligned}\Gamma_{A_1} &= 4\pi\hbar\lambda_\perp^2 \sum_n |\langle\chi_0|\chi'_{\nu_n}\rangle|^2 \delta(\nu_n - \Delta) \\ &= 4\pi\hbar\lambda_\perp^2 F(\Delta),\end{aligned} \tag{3}$$

where $\lambda_\perp$ is the transverse spin-orbit coupling rate, Δ is the energy spacing between $|A_1\rangle$ and $|^1A_1\rangle$, and δ is the Dirac delta function. $|\chi_0\rangle$ is the ground vibrational level of $|A_1\rangle$, and $|\chi'_{\nu_n}\rangle$ are the vibrational levels of $|^1A_1\rangle$ with energies ν_n above that of $|^1A_1\rangle$. We define the vibrational overlap function $F(\Delta) = \overline{|\langle\chi_0|\chi'_\Delta\rangle|^2}\rho(\Delta)$, where the average is over all vibrational levels with energy Δ and $\rho(\Delta)$ is the associated density of states.

At low temperature, the ISC rate from $|E_{1,2}\rangle$ is

$$\begin{aligned}\Gamma_{E_{1,2}} &= 4\pi\hbar^3\lambda_\perp^2 \sum_{n,p,k} \frac{\lambda_{p,k}^2}{\omega_k^2} |\langle\chi_0|\chi'_{\nu_n}\rangle|^2 \delta(\nu_n + \omega_k - \Delta) \\ &= \frac{2}{\pi}\hbar\eta\Gamma_{A_1} \int_0^{\min(\Delta,\Omega)} \omega \frac{F(\Delta-\omega)}{F(\Delta)} d\omega,\end{aligned} \tag{4}$$

where $\lambda_{p,k}$ is the phononic coupling rate for a phonon of polarization p and wave vector k, and

$$J(\omega) = \frac{\pi\hbar}{2} \sum_k \lambda_{E_{1,2},k}^2 \delta(\omega - \omega_k) = \eta\omega^3 \tag{5}$$

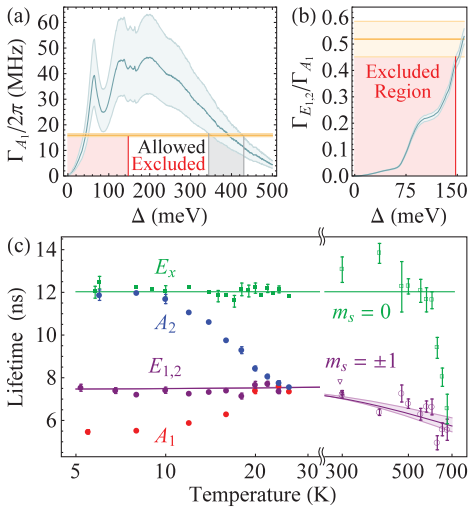

FIG. 4 (color). The results of the ISC model. (a) The range (blue shading) of predicted values of Γ_{A_1} corresponding to the range of possible values of $\lambda_\perp$. The orange line is the measured value of Γ_{A_1}, the black region indicates our extracted value of Δ (the $|A_1\rangle - |^1A_1\rangle$ energy spacing), and the red region indicates the values of Δ that are excluded by the measured $\Gamma_{E_{1,2}}/\Gamma_{A_1}$ ratio. (b) The predicted (blue) and measured (orange) $\Gamma_{E_{1,2}}/\Gamma_{A_1}$ ratio. Because we assume no acoustic phonon cutoff, the blue plot represents an upper bound on the ratio for a given Δ. We can therefore exclude the values of Δ indicated by the red region, which is reproduced in (a). (c) The lifetimes of the $m_s = 0$ (green) and $|m_s| = 1$ (purple) states predicted for a range of temperatures. The data from 295 to 700 K are taken from Refs. [10] (open square and open circle), [9] (open diamond), and [8] (downward triangle).

is the phonon spectral density in the acoustic limit [11] for the polarization that couples $|E_{1,2}\rangle$ with $|A_1\rangle$. We assume a cutoff energy Ω for acoustic phonons.

Because the SO interaction is A_1 symmetric [33], and can therefore only couple states of like symmetry, $|A_2\rangle$ is not SO-coupled to either $|^1A_1\rangle$ or $|^1E_{1,2}\rangle$ [27,28]. Similar symmetry considerations forbid single-phonon coupling between $|A_2\rangle$ and $|A_1\rangle$, so neither the first- nor second-order processes described above can induce ISC decay from $|A_2\rangle$. The lowest-order allowed mechanism would be a third-order process involving two phonons and one SO interaction, but we neither expect nor observe an appreciable ISC transition rate due to such a high-order process.

In Fig. 4(a), we plot the prediction of Eq. (3) as a function of Δ and the value of $\Gamma_{A_1}/2\pi = 16.0 \pm 0.6$ MHz extracted from the fits shown in Fig. 3. The broad range of predicted values of Γ_{A_1} arises from the currently imprecise knowledge of the transverse SO coupling rate $\lambda_\perp$ [34]. The vibrational overlap function is extracted from a previous measurement of the $^3E \rightarrow {}^3A_2$ emission PSB [30]. The intersection of the measured and predicted values of Γ_{A_1} confines Δ to two regions: around 43 meV and from 344 to 430 meV.

We next evaluate $\Gamma_{E_{1,2}}/\Gamma_{A_1}$, which depends only on electron-phonon coupling parameters and the vibronic overlap function, not on the SO coupling rate. We extract $\eta = 2\pi \times (44.0 \pm 2.4)$ MHz meV^{-3}, which parametrizes the electron-phonon coupling strength, from the $|E_x\rangle - |E_y\rangle$ mixing data shown in Fig. 2(a) [16]. In Fig. 4(b), we plot the ratios predicted by Eqs. (3)–(4) [36] and extracted from Fig. 3. We assume no acoustic cutoff energy ($\Omega \rightarrow \infty$) in order to maximize the range of acoustic phonon modes that contribute to $\Gamma_{E_{1,2}}$, making the predicted ratio an upper bound. Even so, we find that the predicted and measured ratios are inconsistent for $\Delta < 148$ meV, which uniquely confines Δ to the region from 344 to 430 meV [37].

We scale our model up to higher temperatures [22] and find that, for this range of Δ, its predictions are consistent with published lifetimes of the $m_s = 0$ and $|m_s| = 1$ ^3E states at temperatures between 295 and 600 K, as shown in Fig. 4(c). An additional decay mechanism, which is not captured by our model of ISC decay, significantly shortens the lifetime of the $m_s = 0$ states above 600 K. This decay mechanism is discussed further in Ref. [22].

We have elucidated, both experimentally and theoretically, the roles that electron-phonon interactions play in NV center dynamics. Further exploration of either of the phonon roles addressed in this Letter may yield intriguing applications. Resonant electron-phonon coupling in the ^3E manifold could be used to optically cool a high-Q diamond resonator [40,41] close to the vibrational ground state [42]. Such efforts would complement the growing interest in using electron-phonon coupling in the $^3A_2$ states to manipulate the electron spin [43,44] or to generate spin-squeezed states of NV ensembles [45]. Further, our understanding of the ISC mechanism may enable efforts to engineer the ISC rate by, for example, applying a large static strain to shift the energy spacings between the spin-triplet and spin-singlet states [3]. Such an advance would provide an across-the-board enhancement to the spin initialization and readout techniques on which room-temperature NV center applications depend. Finally, our experimentally validated ISC model has confined the unknown energy spacing between the ^3E and $|^1A_1\rangle$ states to a region that can be explored in future optical spectroscopy.

The authors would like to thank J. Maze, A. Gali, E. Togan, A. Akimov, D. Sukachev, Q. Unterreithmeier, A. Zibrov, and A. Palyi for stimulating discussions and experimental contributions. This work was supported by the NSF, CUA, DARPA Quiness program, AFOSR MURI, Australian Research Council, Gordon and Betty Moore Foundation, and Element Six. A. K. acknowledges support from the Alexander von Humboldt Foundation.

*mgoldman@physics.harvard.edu

[1] G. Kucsko, P. C. Maurer, N. Y. Yao, M. Kubo, H. J. Noh, P. K. Lo, H. Park, and M. D. Lukin, Nanometre-scale thermometry in a living cell, Nature (London) **500**, 54 (2013).

[2] M. S. Grinolds, S. Hong, P. Maletinsky, L. Luan, M. D. Lukin, R. L. Walsworth, and A. Yacoby, Nanoscale magnetic imaging of a single electron spin under ambient conditions, Nat. Phys. **9**, 215 (2013).

[3] M. W. Doherty, V. V. Struzhkin, D. A. Simpson, L. P. McGuinness, Y. Meng, A. Stacey, T. J. Karle, R. J. Hemley, N. B. Manson, L. C. L. Hollenberg, and S. Prawer, Electronic Properties and Metrology Applications of the Diamond NV^- Center under Pressure, Phys. Rev. Lett. **112**, 047601 (2014).

[4] F. Dolde, H. Fedder, M. W. Doherty, T. Nöbauer, F. Rempp, G. Balasubramanian, T. Wolf, F. Reinhard, L. C. L. Hollenberg, F. Jelezko, and J. Wrachtrup, Electric-field sensing using single diamond spins, Nat. Phys. **7**, 459 (2011).

[5] T. van der Sar, Z. H. Wang, M. S. Blok, H. Bernien, T. H. Taminiau, D. M. Toyli, D. A. Lidar, D. D. Awschalom, R. Hanson, and V. V. Dobrovitski, Decoherence-protected quantum gates for a hybrid solid-state spin register, Nature (London) **484**, 82 (2012).

[6] P. C. Maurer, G. Kucsko, C. Latta, L. Jiang, N. Y. Yao, S. D. Bennett, F. Pastawski, D. Hunger, N. Chisholm, M. Markham, D. J. Twitchen, J. I. Cirac, and M. D. Lukin, Room-temperature quantum bit memory exceeding one second, Science **336**, 1283 (2012).

[7] N. B. Manson, J. P. Harrison, and M. J. Sellars, Nitrogen-vacancy center in diamond: Model of the electronic structure and associated dynamics, Phys. Rev. B **74**, 104303 (2006).

[8] A. Batalov, C. Zierl, T. Gaebel, P. Neumann, I.-Y. Chan, G. Balasubramanian, P. R. Hemmer, F. Jelezko, and J. Wrachtrup, Temporal Coherence of Photons Emitted by Single Nitrogen-Vacancy Defect Centers in Diamond Using Optical Rabi-Oscillations, Phys. Rev. Lett. **100**, 077401 (2008).

[9] L. Robledo, H. Bernien, T. van der Sar, and R. Hanson, Spin dynamics in the optical cycle of single nitrogen-vacancy centres in diamond, New J. Phys. **13**, 025013 (2011).

[10] D. M. Toyli, D. J. Christle, A. Alkauskas, B. B. Buckley, C. G. Van de Walle, and D. D. Awschalom, Measurement and Control of Single Nitrogen-Vacancy Center Spins above 600 K, Phys. Rev. X **2**, 031001 (2012).

[11] K.-M. C. Fu, C. Santori, P. E. Barclay, L. J. Rogers, N. B. Manson, and R. G. Beausoleil, Observation of the Dynamic Jahn-Teller Effect in the Excited States of Nitrogen-Vacancy Centers in Diamond, Phys. Rev. Lett. **103**, 256404 (2009).

[12] F. Kaiser, V. Jacques, A. Batalov, P. Siyushev, F. Jelezko, and J. Wrachtrup, Polarization properties of single photons emitted by nitrogen-vacancy defect in diamond at low temperature, arXiv:0906.3426.

[13] L. Robledo, H. Bernien, I. van Weperen, and R. Hanson, Control and Coherence of the Optical Transition of Single Nitrogen Vacancy Centers in Diamond, Phys. Rev. Lett. **105**, 177403 (2010).

[14] H. Bernien, B. Hensen, W. Pfaff, G. Koolstra, M. S. Blok, L. Robledo, T. H. Taminiau, M. Markham, D. J. Twitchen, L. Childress, and R. Hanson, Heralded entanglement between solid-state qubits separated by three metres, Nature (London) **497**, 86 (2013).

[15] P. Siyushev, F. Kaiser, V. Jacques, I. Gerhardt, S. Bischof, H. Fedder, J. Dodson, M. Markham, D. Twitchen, F. Jelezko, and J. Wrachtrup, Monolithic diamond optics for single photon detection, Appl. Phys. Lett. **97**, 241902 (2010).

[16] See Supplemental Material at http://link.aps.org/supplemental/10.1103/PhysRevLett.114.145502, which includes Refs. [17–20], for detailed discussions of experimental methods and data analysis techniques.

[17] L. C. Bassett, F. J. Heremans, C. G. Yale, B. B. Buckley, and D. D. Awschalom, Electrical Tuning of Single Nitrogen-Vacancy Center Optical Transitions Enhanced by Photoinduced Fields, Phys. Rev. Lett. **107**, 266403 (2011).

[18] F. Jelezko and J. Wrachtrup, Read-out of single spins by optical spectroscopy, J. Phys. Condens. Matter **16**, R1089 (2004).

[19] J.-P. Tetienne, L. Rondin, P. Spinicelli, M. Chipaux, T. Debuisschert, J.-F. Roch, and V. Jacques, Magnetic-field-dependent photodynamics of single NV defects in diamond: an application to qualitative all-optical magnetic imaging, New J. Phys. **14**, 103033 (2012).

[20] L. Robledo, L. Childress, H. Bernien, B. Hensen, P. F. A. Alkemade, and R. Hanson, High-fidelity projective read-out of a solid-state spin quantum register, Nature (London) **477**, 574 (2011).

[21] C. Cohen-Tannoudji, J. Dupont-Roc, and G. Grynberg, *Atom-Photon Interactions: Basic Processes and Applications*, 1st ed. (Wiley-VCH, New York, 1992).

[22] M. L. Goldman, M. W. Doherty, A. Sipahigil, N. Y. Yao, S. D. Bennett, N. B. Manson, A. Kubanek, and M. D. Lukin, State-selective intersystem crossing in nitrogen-vacancy centers, Phys. Rev. B **91**, 165201 (2015).

[23] Although the one-phonon process contributes negligibly in this experiment, it may cause significant mixing in NV centers, such as those formed by nitrogen implantation or placed inside nanofabricated structures, where damage to the local crystalline structure may induce a large strain splitting. We note that this linear temperature scaling may be evident in the result of a previous measurement of phonon-induced mixing, which used NV centers with strain splittings of 8 to 81 GHz [11].

[24] M. W. Doherty, N. B. Manson, P. Delaney, F. Jelezko, J. Wrachtrup, and L. C. L. Hollenberg, The nitrogen-vacancy colour centre in diamond, Phys. Rep. **528**, 1 (2013).

[25] G. D. Fuchs, V. V. Dobrovitski, R. Hanson, A. Batra, C. D. Weis, T. Schenkel, and D. D. Awschalom, Excited-State Spectroscopy Using Single Spin Manipulation in Diamond, Phys. Rev. Lett. **101**, 117601 (2008).

[26] L. J. Rogers, R. L. McMurtrie, M. J. Sellars, and N. B. Manson, Time-averaging within the excited state of the nitrogen-vacancy centre in diamond, New J. Phys. **11**, 063007 (2009).

[27] M. W. Doherty, N. B. Manson, P. Delaney, and L. C. L. Hollenberg, The negatively charged nitrogen-vacancy centre in diamond: the electronic solution, New J. Phys. **13**, 025019 (2011).

[28] J. R. Maze, A. Gali, E. Togan, Y. Chu, A. Trifonov, E. Kaxiras, and M. D. Lukin, Properties of nitrogen-vacancy centers in diamond: the group theoretic approach, New J. Phys. **13**, 025025 (2011).

[29] V. M. Huxter, T. A. A. Oliver, D. Budker, and G. R. Fleming, Vibrational and electronic dynamics of nitrogen-vacancy centres in diamond revealed by two-dimensional ultrafast spectroscopy, Nat. Phys. **9**, 744 (2013).

[30] P. Kehayias, M. W. Doherty, D. English, R. Fischer, A. Jarmola, K. Jensen, N. Leefer, P. Hemmer, N. B. Manson, and D. Budker, Infrared absorption band and vibronic structure of the nitrogen-vacancy center in diamond, Phys. Rev. B **88**, 165202 (2013).

[31] V. M. Acosta, A. Jarmola, E. Bauch, and D. Budker, Optical properties of the nitrogen-vacancy singlet levels in diamond, Phys. Rev. B **82**, 201202 (2010).

[32] G. Davies and M. F. Hamer, Optical studies of the 1.945 eV vibronic band in diamond, Proc. R. Soc. A **348**, 285 (1976).

[33] A. Lenef and S. C. Rand, Electronic structure of the N-V center in diamond: Theory, Phys. Rev. B **53**, 13441 (1996).

[34] The axial SO coupling rate $\lambda_{||} = 5.33 \pm 0.03$ GHz is known [35], but the precise value of $\lambda_{\perp}/\lambda_{||} \approx 1$ remains an open question. As explained in Ref. [22], we have selected $\lambda_{\perp}/\lambda_{||} = 1.2 \pm 0.2$ as a reasonable confidence interval.

[35] L. C. Bassett, F. J. Heremans, D. J. Christle, C. G. Yale, G. Burkard, B. B. Buckley, and D. D. Awschalom, Ultrafast optical control of orbital and spin dynamics in a solid-state defect, Science **345**, 1333 (2014).

[36] The value of $\Gamma_{E_{1,2}}$ calculated in Fig. 4(b) includes a correction to Eq. (4) due to a second-order ISC process that uses $|^1E_{1,2}\rangle$ as intermediate states instead of $|A_1\rangle$. This correction, which is described explicitly in Ref. [22], lowers $\Gamma_{E_{1,2}}/\Gamma_{A_1}$ by 21% at $\Delta = 148$ meV.

[37] In this region, we find that the predicted and measured ratios match for cutoff energies of 74 to 93 meV. These values, which are below the Debye energy (194 meV [38]) and close to the energies of the quasilocal phonon modes that dominate the ^3E (64 meV [30,39]) and $|^1A_1\rangle$ (71 meV [32]) PSBs, are physically reasonable.

[38] A. Bosak and M. Krisch, Phonon density of states probed by inelastic x-ray scattering, Phys. Rev. B **72**, 224305 (2005).

[39] G. Davies, Vibronic spectra in diamond, J. Phys. C **7**, 3797 (1974).

[40] P. Ovartchaiyapong, L. M. A. Pascal, B. A. Myers, P. Lauria, and A. C. Bleszynski Jayich, High quality factor single-crystal diamond mechanical resonators, Appl. Phys. Lett. **101**, 163505 (2012).

[41] Y. Tao, J. M. Boss, B. A. Moores, and C. L. Degen, Single-crystal diamond nanomechanical resonators with quality factors exceeding one million, Nat. Commun. **5**, 3638 (2014).

[42] K. V. Kepesidis, S. D. Bennett, S. Portolan, M. D. Lukin, and P. Rabl, Phonon cooling and lasing with nitrogen-vacancy centers in diamond, Phys. Rev. B **88**, 064105 (2013).

[43] E. R. MacQuarrie, T. A. Gosavi, N. R. Jungwirth, S. A. Bhave, and G. D. Fuchs, Mechanical Spin Control of Nitrogen-Vacancy Centers in Diamond, Phys. Rev. Lett. **111**, 227602 (2013).

[44] P. Ovartchaiyapong, K. W. Lee, B. A. Myers, and A. C. Bleszynski Jayich, Dynamic strain-mediated coupling of a single diamond spin to a mechanical resonator, Nat. Commun. **5**, 4429 (2014).

[45] S. D. Bennett, N. Y. Yao, J. Otterbach, P. Zoller, P. Rabl, and M. D. Lukin, Phonon-Induced Spin-Spin Interactions in Diamond Nanostructures: Application to Spin Squeezing, Phys. Rev. Lett. **110**, 156402 (2013).